Role of typical elements in $Nd_2Fe_{14}X$ (X = B, C, N, O, F)

Yasutomi Tatetsu,[1,2,*] Yosuke Harashima,[2,3,†] Takashi Miyake,[2,3,4] and Yoshihiro Gohda[1,2]
[1]*Department of Materials Science and Engineering, Tokyo Institute of Technology, Yokohama 226-8502, Japan*
[2]*ESICMM, National Institute for Materials Science, Tsukuba 305-0047, Japan*
[3]*CD-FMat, National Institute of Advanced Industrial Science and Technology, Tsukuba 305-8568, Japan*
[4]*CMI², MaDIS, National Institute for Materials Science, Tsukuba 305-0047, Japan*

(Received 9 February 2018; revised manuscript received 24 May 2018; published 31 July 2018)

The magnetic properties and structural stability of $Nd_2Fe_{14}X$ (X = B, C, N, O, F) are theoretically studied by first-principles calculations focusing on the role of X. We find that B reduces the magnetic moment (per formula unit) and magnetization (per volume) in $Nd_2Fe_{14}B$. The crystal-field parameter $A_2^0\langle r^2\rangle$ of Nd is not enhanced either, suggesting that B has minor roles in the uniaxial magnetocrystalline anisotropy of Nd. These findings are in contrast to the long-held belief that B works positively for the magnetic properties of $Nd_2Fe_{14}B$. As X changes from B to C, N, O, and F, both the magnetic properties and stability vary significantly. The formation energies of $Nd_2Fe_{14}X$ and α-Fe relative to that of $Nd_2Fe_{17}X$ are negative for X = B and C, whereas they are positive when X = N, O, and F. This indicates that B plays an important role in stabilizing the $Nd_2Fe_{14}B$ phase.

DOI: 10.1103/PhysRevMaterials.2.074410

I. INTRODUCTION

Back in the 1970s, Sm_2Co_{17} was the strongest known hard magnetic compound. As Co is an expensive element whereas Fe is relatively cheap, developing iron-based permanent magnets was required. Sm_2Fe_{17}, more generally known as R_2Fe_{17} where R represents rare-earth elements, was a natural choice. However, the Curie temperature T_c of R_2Fe_{17} is too low for practical applications. For example, T_c of Nd_2Fe_{17} is about 330 K [1–3]. Sagawa came up with the following idea in order to raise the T_c of R_2Fe_{17}: The introduction of light elements, such as B and C, at the interstitial region in R_2Fe_{17} would expand the volume of R_2Fe_{17} [4,5]. This volume expansion could make the ferromagnetism stronger by the magnetovolume effect; consequently T_c would go up. He added B to Nd_2Fe_{17} based on this idea, and successfully developed Nd-Fe-B magnets having a T_c of 585 K [4,6]. It is important to note that the main phase of Nd-Fe-B magnets is $Nd_2Fe_{14}B$, not $Nd_2Fe_{17}B$. In particular, the effect of B on the magnetization, magnetic moments, and magnetocrystalline anisotropy of $Nd_2Fe_{14}B$ was unclear due to the reasons described in the following two paragraphs.

After the Nd-Fe-B magnet was developed, the role of B in the magnetism of $Nd_2Fe_{14}B$ was studied theoretically [7–9]. Kanamori pointed out the importance of the p-d hybridization between B and Fe sites. The magnetic moment of Fe in the vicinity of B should be suppressed. It is called cobaltization. The cobaltized Fe (pseudo Co) can enhance the magnetic moment of the surrounding Fe due to the d-d hybridization between pseudo Co and Fe, as in Fe-Co alloys [10,11]. It has been believed for decades that when these chemical effects, owing to hybridizations, are summed up, the total magnetic moment of $Nd_2Fe_{14}B$ increases by B.

Asano and Yamaguchi studied the magnetic properties of $Y_2Fe_{14}B$ and the hypothetical compound Y_2Fe_{14} through first-principles calculations [12,13]. Their results show (i) the magnetic moment of Fe, at the nearest neighbor of B in $Y_2Fe_{14}B$, is reduced by the cobaltization, (ii) the magnetic moment of Fe at the nearest neighbor of pseudo Co is enhanced, and (iii) the effect of B is slightly negative on the magnetization in $Y_2Fe_{14}B$. Therefore, $Y_2Fe_{14}B$ has smaller total magnetic moment than Y_2Fe_{14}. However, they optimized only lattice parameters within the atomic-sphere approximation, and internal coordinates were fixed. Moreover, magnetovolume effects and chemical effects were not distinguished. Therefore, the effects of B on the magnetism in $R_2Fe_{14}B$ still needs to be clarified.

In this study, we systematically investigate the influence of B on the electronic states and magnetism of $Nd_2Fe_{14}B$ through first-principles calculations. We find that the total magnetic moment (per formula unit) and magnetization (per volume) of $Nd_2Fe_{14}B$ decrease by the addition of B. This result is analyzed in terms of the chemical effect and magnetovolume effect caused by B. The local magnetic moment at each Fe site is computed and is discussed in connection with cobaltization. We also study $Nd_2Fe_{14}X$, where X represents C, N, O, and F, in order to investigate the effects of the X element on the magnetization, magnetocrystalline anisotropy, and stability of $Nd_2Fe_{14}X$.

II. COMPUTATIONAL METHODS

We perform first-principles calculations of $Nd_2Fe_{14}X$ within density functional theory. We use the computational package OPENMX, which is based on pseudopotentials and pseudo-atomic-orbital basis functions [14]. The basis set of Nd, Fe, and X is $s2p2d2$, and the cutoff radii of these atoms are 8.0, 6.0, and 7.0 a.u., respectively. For semicore states, we treat $3s$ and $3p$ orbitals as valence electrons in Fe, and the same for $5s$ and $5p$ in Nd. An open-core (OC) pseudopotential

*tatetsu.y.aa@m.titech.ac.jp
†yosuke-harashima@aist.go.jp

is used for Nd atoms, where $4f$ electrons are treated as spin-polarized core electrons. The calculation for valence electronic states does not include the spin-orbit interaction. We adopt the Perdew-Burke-Ernzerhof exchange-correlation functional in the generalized gradient approximation [15]. The lattice parameters and atomic positions of $Nd_2Fe_{14}X$ are all relaxed. For the convergence criteria, the maximum force on each atom and the total energy are 10^{-4} hartree/bohr and 10^{-7} hartree, respectively. Spin collinear structures are assumed in all the calculations for $Nd_2Fe_{14}X$. The cutoff energy is 500 Ry, and $8 \times 8 \times 6$ k-point meshes are adopted for all the calculations.

The magnetic moment is estimated from the spin moment of valence electrons and the contribution of Nd $4f$ electrons $g_J J = 3.273\mu_B$, where g_J is the Lande g-factor and J is the total angular momentum of Nd $4f$ electrons. The magnetization is calculated from the total magnetic moment of $Nd_2Fe_{14}X$ by dividing volume V (see Appendix B) and multiplying the Bohr magneton μ_B. The crystal-field parameters A_l^m of Nd are calculated by using the computational package QMAS, which is based on the projector augmented-wave method [16]. See Refs. [17,18] for more details.

We note that there are different notations for the Wyckoff positions of $Nd_2Fe_{14}B$ [19–22]. Throughout this paper, the notation given in Refs. [19,22] is used.

III. RESULTS AND DISCUSSION

A. Roles of B in $Nd_2Fe_{14}B$

We calculate the magnetic moment and magnetization of $Nd_2Fe_{14}B$ and Nd_2Fe_{14} in order to investigate the effects of B on $Nd_2Fe_{14}B$. Nd_2Fe_{14} is a hypothetical compound in which the X site is empty and all the atomic positions and lattice parameters are optimized. For comparison, we also study $Nd_2Fe_{14}B_0$, in which the lattice parameters and atomic positions are the same as those of $Nd_2Fe_{14}B$, but B has been removed. These hypothetical compounds are introduced in order to distinguish the magnetovolume and chemical effects on the magnetic moment and magnetization of $Nd_2Fe_{14}B$. The results are listed in Table I. The calculated magnetic moment of $Nd_2Fe_{14}B$ is consistent with the experimental value of $37.9\mu_B$/f.u. measured at 4.2 K [23]. From the comparison between $Nd_2Fe_{14}B$ and Nd_2Fe_{14}, we find that the introduction of B decreases both the magnetic moment and magnetization of $Nd_2Fe_{14}B$. The magnetovolume effect of B can be evaluated by comparing magnetization of $Nd_2Fe_{14}B_0$ with that of Nd_2Fe_{14}. The difference between the two comes solely from the structural change. The magnetic moment of $Nd_2Fe_{14}B_0$ is enhanced by 1% compared to that of Nd_2Fe_{14}. When it is converted to magnetization, however, the magnetization is reduced by 0.017 T due to the volume expansion. By comparing $Nd_2Fe_{14}B$ and $Nd_2Fe_{14}B_0$, we can see that the chemical effect of B is negative on both the magnetic moment and magnetization. The magnitude is larger in the chemical effect than in the magnetovolume effect. This leads to a decrease of the magnetic moment caused by B. This result gives us a different insight from that of the current belief that B enhances the magnetic moment and magnetization of $Nd_2Fe_{14}B$.

TABLE I. The magnetic moment m (μ_B/f.u.) and magnetization $\mu_0 M$ (T) of $Nd_2Fe_{14}B$, $Nd_2Fe_{14}B_0$, and Nd_2Fe_{14}.

	m (μ_B/f.u.)	$\mu_0 M$ (T)
$Nd_2Fe_{14}B$	37.42	1.86
$Nd_2Fe_{14}B_0$	38.87	1.93
Nd_2Fe_{14}	38.43	1.95

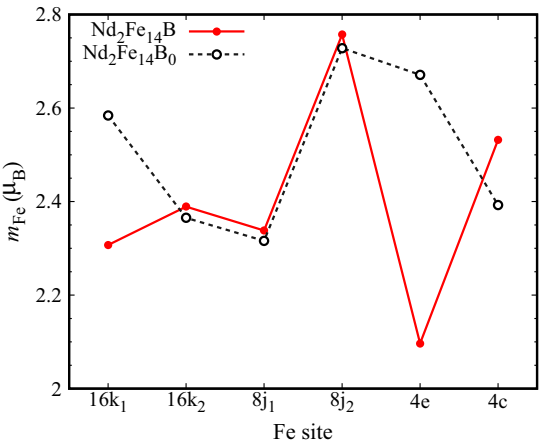

FIG. 1. The local magnetic moments of Fe at each site m_{Fe} in $Nd_2Fe_{14}B$ (closed red circles) and $Nd_2Fe_{14}B_0$ (open black circles). The site notation follows Refs. [19,22] (see also Fig. 9). Lines are provided as a visual guide.

The local magnetic moments of Fe at each site in $Nd_2Fe_{14}B$ and $Nd_2Fe_{14}B_0$ are shown in Fig. 1. These calculated magnetic moments are consistent with that of experimental values by neutron-scattering studies [23–25]. By following the concept of cobaltization, one can expect the decrease of the Fe magnetic moment at the neighbors of B. The local magnetic moment at the Fe sites near the pseudo Co, in turn, can be expected to be enhanced due to the presence of pseudo Co. The Fe atoms at the $16k_1$ and $4e$ sites are the first and second neighbors of B, and the distances between these Fe atoms and B are about 2.1 Å. Therefore, these Fe atoms become pseudo Co. In fact, the decrease of the Fe local moments is actually seen at these two sites in Fig. 1. All the other Fe sites are near the pseudo Co; thus, we can see the small enhancement of the magnetic moment at these sites. The reduction at the pseudo-Co sites is larger than the increase at the neighbors of the pseudo-Co sites in magnitude. To sum up, B reduces the magnetic moment and magnetization of $Nd_2Fe_{14}B$.

Next, we examine how the magnetocrystalline anisotropy of $Nd_2Fe_{14}B$ around room temperature is influenced by the added B. To do this, we analyze the crystal-field parameter $A_2^0\langle r^2\rangle$ of Nd. The magnetocrystalline anisotropy energy E_{MAE} can be expressed as

$$E_{MAE} = K_1 \sin^2\theta + K_2 \sin^4\theta + \cdots . \quad (1)$$

In crystal-field theory, when J and M_J excitations are not considered, K_1 of $Nd_2Fe_{14}B$ is simply approximated by considering only the lowest-order term as

$$K_1 = -3J\left(J - \frac{1}{2}\right)\Theta_2^0 A_2^0\langle r^2\rangle, \quad (2)$$

where J is the total angular momentum quantum number, M_J is the total magnetic quantum number, and $A_2^0\langle r^2\rangle$ is a crystal-field parameter. Since K_1 decreases with increasing temperature mainly due to M_J excitations, Eq. (2) is used to help understand the qualitative relationship between the different K_1 values. The crystal-field parameter of Nd can be calculated from the effective potential obtained through first-principles calculations. Although the magnetocrystalline anisotropy energy includes higher-order contributions, for example, $A_4^0\langle r^4\rangle$ and $A_6^0\langle r^6\rangle$, the magnetocrystalline anisotropy of Nd at high temperatures can be discussed by considering only the lowest-order contribution [26,27], because the higher terms of $A_l^0\langle r^l\rangle$ decrease rapidly compared to $A_2^0\langle r^2\rangle$ with increasing temperature [28,29]. The higher-order crystal-field parameters are discussed in Appendix C. There are two different Wyckoff positions for Nd, labeled as Nd($4f$) and Nd($4g$). The calculated $A_2^0\langle r^2\rangle$ are 220 K at Nd($4f$) and 330 K at Nd($4g$) for $Nd_2Fe_{14}B$. Those for Nd_2Fe_{14} are 206 K at Nd($4f$) and 434 K at Nd($4g$). The calculated K_1 values from substituting these $A_2^0\langle r^2\rangle$ into Eq. (2) are 6.6, 9.9, 6.2, and 13.0 meV, respectively. This result indicates that Nd_2Fe_{14} already shows uniaxial anisotropy, and the presence of B has a minor impact on the magnetocrystalline anisotropy. In this connection, the magnetic anisotropy energy of Nd is larger than that of Fe ($-0.4\sim0.2$ meV) in $Nd_2Fe_{14}B$ by two orders of magnitude [30,31].

From the above results, the advantage of adding B cannot be seen, so far, since its addition does not seem to play an important role in terms of enhancing the magnetization and magnetocrystalline anisotropy of $Nd_2Fe_{14}B$. What is the benefit of adding B in $Nd_2Fe_{14}B$? A probable role is to stabilize the structure of $Nd_2Fe_{14}B$. In order to confirm that, we examine the stability of $Nd_2Fe_{14}B$. We choose $Nd_2Fe_{17}B$ as a reference system from the historical reason that Sagawa intended to insert B into Nd_2Fe_{17}, as explained in Sec. I. We define the formation energy ΔE as follows:

$$\Delta E \equiv (E[Nd_2Fe_{14}B] + 3\mu[Fe]) - E[Nd_2Fe_{17}B] \quad (3)$$

$$= \{(E[Nd_2Fe_{14}B] + 3\mu[Fe]) - (E[Nd_2Fe_{17}] + \mu[B])\} - \{E[Nd_2Fe_{17}B] - (E[Nd_2Fe_{17}] + \mu[B])\}. \quad (4)$$

Here, $E[Nd_2Fe_{14}B]$, $E[Nd_2Fe_{17}B]$, and $E[Nd_2Fe_{17}]$ denote the total energy of $Nd_2Fe_{14}B$, $Nd_2Fe_{17}B$, and Nd_2Fe_{17} per formula unit, respectively, while μ[Fe] and μ[B] represent chemical potentials corresponding to the total energy of α-Fe and α-B per atom, respectively. Equation (4) shows the difference between the formation energies of $Nd_2Fe_{14}B$ and the system in which one B atom is added in Nd_2Fe_{17} per formula unit. The resultant formation energy is $\Delta E = -1.208$ eV/f.u. We calculate the formation energies $E_{\rm form}$ of $Nd_2Fe_{14}B$ and Nd_2Fe_{14} with the following equations:

$$E_{\rm form}[Nd_2Fe_{14}B] = E[Nd_2Fe_{14}B] - (2\mu[\text{dhcp-Nd}] + 14\mu[\text{bcc-Fe}] + \mu[B]),$$

$$E_{\rm form}[Nd_2Fe_{14}] = E[Nd_2Fe_{14}] - (2\mu[\text{dhcp-Nd}] + 14\mu[\text{bcc-Fe}]). \quad (5)$$

Here, $E[Nd_2Fe_{14}B]$ and $E[Nd_2Fe_{14}]$ represent the total energies of $Nd_2Fe_{14}B$ and Nd_2Fe_{14}, while μ[dhcp-Nd], μ[bcc-Fe], and μ[B] are the chemical potentials as in Eq. (4). The calculated $E_{\rm form}[Nd_2Fe_{14}B]$ and $E_{\rm form}[Nd_2Fe_{14}]$ are -1.20 and 0.51 eV/f.u., respectively, which indicates that $Nd_2Fe_{14}B$ is more stable than Nd_2Fe_{14}. From these formation-energy analyses of $Nd_2Fe_{14}B$, we conclude that B in $Nd_2Fe_{14}B$ stabilizes the structure of $Nd_2Fe_{14}B$.

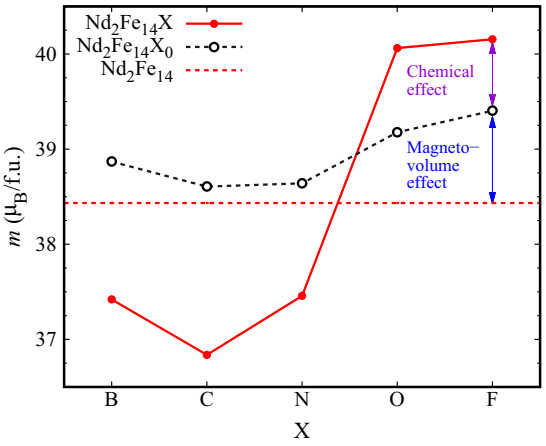

FIG. 2. The X dependence of the magnetic moment m (μ_B). The closed red circles are data for $Nd_2Fe_{14}X$ and the open black circles are data for $Nd_2Fe_{14}X_0$. The broken red line illustrates the magnetic moment of Nd_2Fe_{14}.

B. Comparison with $Nd_2Fe_{14}X$ (X = C, N, O, F)

In this section, we systematically compare the magnetization, magnetic moments, magnetocrystalline anisotropy, and stability of $Nd_2Fe_{14}X$ with the results of $Nd_2Fe_{14}B$ when X is C, N, O, and F. Figure 2 illustrates the magnetic moment of $Nd_2Fe_{14}X$. By comparing the broken red line of Nd_2Fe_{14} with the open black circles of $Nd_2Fe_{14}X_0$, we can see that the magnetovolume effect works positively to increase the magnetic moment in all the cases studied here. This tendency is proportional to the volume expansion caused by the X elements (see Table II). Similarly, we can evaluate the chemical effects of the X elements on the magnetic moment by comparing the black circles with the red circles of $Nd_2Fe_{14}X$, because the structures of $Nd_2Fe_{14}X_0$ are fixed to those of $Nd_2Fe_{14}X$. The difference between these two systems is entirely the absence or presence of the X elements. We can see that the chemical effect strongly depends on X. When X = B, C, and N, the chemical effect is negative, while it is positive when X = O and F. Similar trends for the magnetovolume and chemical effects have been reported before in $NdFe_{11}TiX$ [18] (also in a simpler system,

TABLE II. The calculated lattice constants and volumes of $Nd_2Fe_{14}X$ and Nd_2Fe_{14} (denoted as E). The lattice constants a and c are for a conventional unit cell described in angstroms. The volumes V are per formula unit described in Å^3.

X =	B	C	N	O	F	E
a (Å)	8.791	8.805	8.816	8.858	8.833	8.760
c (Å)	12.141	11.934	11.925	12.154	12.561	11.989
V (Å^3/f.u.)	234.6	231.3	231.7	238.4	245.0	230.0

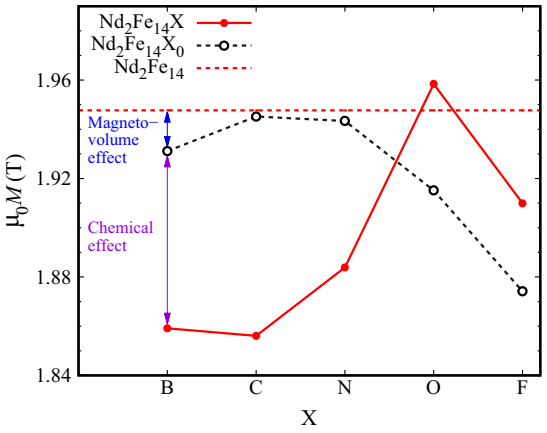

FIG. 3. The X dependence of magnetization $\mu_0 M$ (T). The closed red circles and the open black circles represent the magnetization of $Nd_2Fe_{14}X$ and $Nd_2Fe_{14}X_0$, respectively. Lines are a visual guide. For reference, the broken red line is the magnetization of Nd_2Fe_{14}.

Fe_4X [32]). A difference between $Nd_2Fe_{14}X$ and $NdFe_{11}TiX$ is seen in the total magnetic moment for $X = N$. The total magnetic moment is suppressed in the former, whereas it is enhanced in the latter; namely, $NdFe_{11}TiN$ has a larger magnetic moment than $NdFe_{11}Ti$.

The above results are converted to the magnetization in Fig. 3. The magnetization is lower in $Nd_2Fe_{14}X$ than in Nd_2Fe_{14}, except when $X = O$. From the comparison between Nd_2Fe_{14} and $Nd_2Fe_{14}X_0$, we can see that the magnetovolume effect is negative in all cases, which is in contrast to the positive magnetovolume effect for $NdFe_{11}TiX$ [18]. Especially, the negative effect is large when X is O or F. On the other hand, the chemical effect is negative when X is B, C, or N, but positive when X is O or F. The chemical effect plays an important role in enhancing the magnetization of $Nd_2Fe_{14}O$.

Figure 4 illustrates the local magnetic moments at each Fe site in $Nd_2Fe_{14}X$ and $Nd_2Fe_{14}X_0$. We can see the increase of the magnetic moments at $16k_1$ and $4e$ sites when X changes from N to O. This enhancement arises from the p-d hybridization between O and Fe [12,13,18]. Figure 5 shows the projected density of states on N and O. In the case of $X = N$, there is a peak above the Fermi level in the majority-spin channel. It comes from the antibonding state between N $2p$ and Fe $3d$ orbitals. The corresponding peak in the minority-spin channel is observed at higher energy (2–3 eV above the Fermi level). In the case of $X = O$, the state is pulled down and is occupied in the majority-spin channel. This spin-dependent occupancy makes a distinction in magnetization between the cases of N and O. A similar increase is observed in the local moment of the Fe($8j$) sites in $NdFe_{11}TiX$ when $X = C$ and N [18]. The difference can be explained as follows: In $NdFe_{11}TiX$, the antibonding state can be constituted from π bonds with surrounding Fe atoms due to the highly symmetric environment at X (even though Ti slightly breaks the symmetry). In $Nd_2Fe_{14}X$, one X-Fe π bond hybridizes with other Fe atoms via a σ bond. This σ bond is stronger than the π bond and makes the level of the antibonding state higher. Consequently, the antibonding state is shifted down to the Fermi level and occupied for an element having deeper $2p$ level, that is, O in $Nd_2Fe_{14}X$.

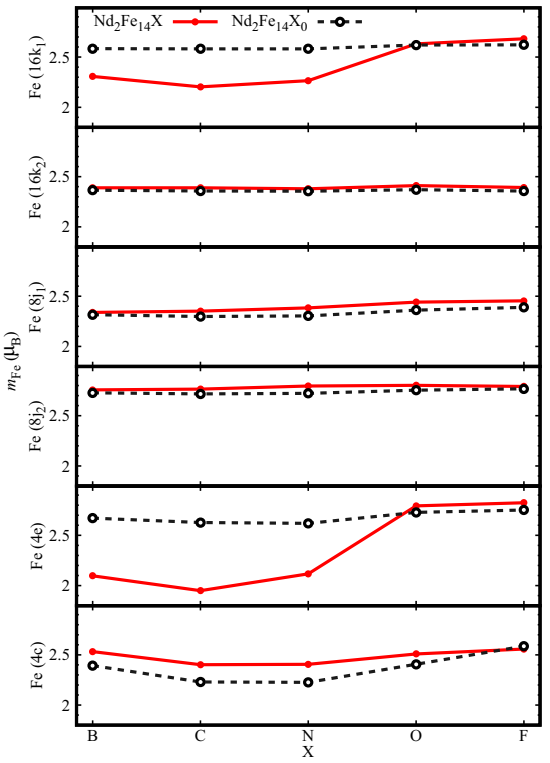

FIG. 4. The X dependence of the local magnetic moment of $Nd_2Fe_{14}X$. The closed red circles are data for $Nd_2Fe_{14}X$ and the open black circles are data for $Nd_2Fe_{14}X_0$. The site notation follows Refs. [19,22].

Figure 6 illustrates the dependence of the crystal-field parameter $A_2^0\langle r^2\rangle$ of Nd on X. The values of both Nd($4f$) and Nd($4g$) sites are shown. They are positive in all cases and $A_2^0\langle r^2\rangle$ increases as the atomic number of X increases [except for Nd($4g$) at $X = O$]. This implies that $Nd_2Fe_{14}X$ has uniaxial anisotropy at high temperatures and that the anisotropy is enhanced as the atomic number increases. $A_2^0\langle r^2\rangle$ of Nd($4f$) in $Nd_2Fe_{14}X_0$ also increases from $X = C$ to F. The chemical effect on Nd($4f$) is large in magnitude and seems to be similar among $X = C$, N, O, and F. For Nd($4g$) in $Nd_2Fe_{14}X_0$, $A_2^0\langle r^2\rangle$ is almost constant and the X dependence in $A_2^0\langle r^2\rangle$ of Nd($4g$) is mainly due to the chemical effect.

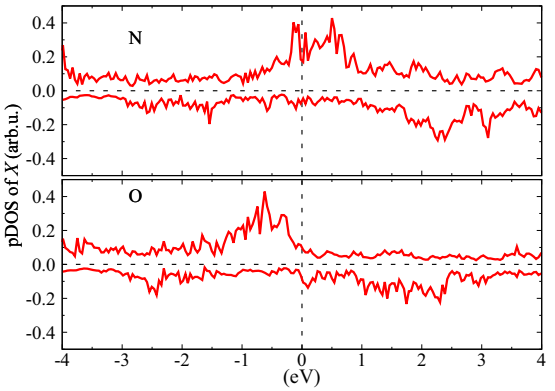

FIG. 5. The local density of states of N in $Nd_2Fe_{14}N$ and O in $Nd_2Fe_{14}O$.

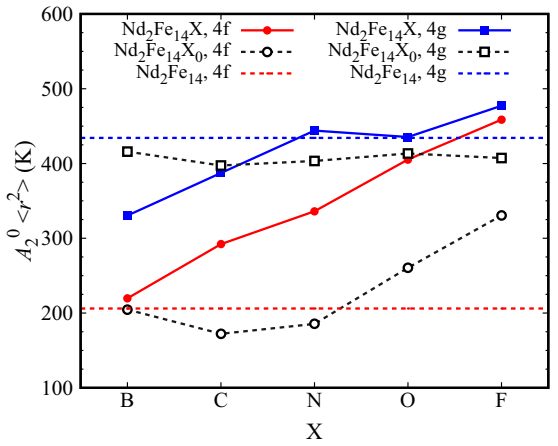

FIG. 6. $A_2^0\langle r^2\rangle$ of $Nd_2Fe_{14}X$ and $Nd_2Fe_{14}X_0$. The closed red circles are data for $Nd_2Fe_{14}X$ and open black circles for $Nd_2Fe_{14}X_0$. The horizontal broken red line denotes data for Nd_2Fe_{14}. Lines are a guide to the eye.

Figure 7 shows the formation energies of $Nd_2Fe_{14}X$ as a function of the X elements calculated with Eq. (3), but B is replaced with C, N, O, and F. $Nd_2Fe_{14}X$ is stable when X is B or C, but not when X is N, O, or F. In other words, $Nd_2Fe_{17}X$ is more stable when X is N, O, or F. These results are in good agreement with the fact that $Nd_2Fe_{14}B$ and $Nd_2Fe_{17}N_x$ ($0 < x \lesssim 3$) can be stably synthesized in experiments.

IV. CONCLUSIONS

The roles of added B in $Nd_2Fe_{14}B$ have been carefully investigated by first-principles calculations. As reported in previous studies, cobaltized Fe atoms can be seen in $Nd_2Fe_{14}B$. However, magnetization is not enhanced by the added B. We clarify that both the chemical and magnetovolume effects work negatively on the magnetization of $Nd_2Fe_{14}B$. The magnetocrystalline anisotropy discussed by the crystal-field parameter $A_2^0\langle r^2\rangle$ has a minor effect from the addition of B. We also systematically examined the effects of the X elements on the magnetism in $Nd_2Fe_{14}X$ through first-principles calculations. The enhancement in the magnetization is observed only for $X = O$. The crystal-field parameter $A_2^0\langle r^2\rangle$ has a tendency to increase as the atomic number of X increases. The stability of $Nd_2Fe_{14}X$ was also calculated by comparing the formation energies to that of $Nd_2Fe_{17}X$. The formation energies of $Nd_2Fe_{14}B$ and $Nd_2Fe_{14}C$ are negative relative to $Nd_2Fe_{17}X$, while $Nd_2Fe_{14}N$, $Nd_2Fe_{14}O$, and $Nd_2Fe_{14}F$ are not energetically stable. This result is consistent with experimental results.

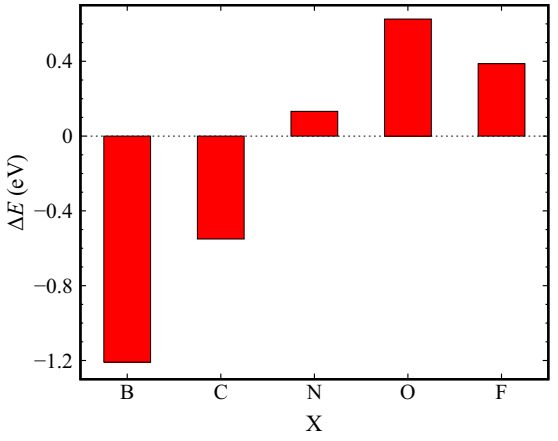

FIG. 7. The formation energy of $Nd_2Fe_{14}X$ defined by Eq. (3) with replacement of B with C, N, O, and F.

ACKNOWLEDGMENTS

We thank Dr. S. Hirosawa, Dr. T. Nakamura, and Dr. T. Fukazawa for his fruitful and stimulating discussion. This work was supported by the Elements Strategy Initiative Project under the auspices of MEXT, by the "Materials research by Information Integration" Initiative (MI^2I) project of the Support Program for Starting Up Innovation Hub from Japan Science and Technology Agency (JST), and also by MEXT as a social and scientific priority issue [Creation of new functional Devices and high-performance Materials to Support next-generation Industries (CDMSI)] to be tackled by using post-K computer, as well as JSPS KAKENHI Grant No. 17K04978. The calculations were partly carried out by using supercomputers at ISSP, The University of Tokyo, and TSUBAME, Tokyo Institute of Technology, the supercomputer of ACCMS, Kyoto University, and also by the K computer, RIKEN (Projects No. hp160227, No. hp170100, and No. hp170269).

APPENDIX A: DENSITY OF STATES OF $Nd_2Fe_{14}B$

We analyzed the density of states (DOS) of $Nd_2Fe_{14}B$ in order to check the sensitivity of the magnetic and electronic structures of $Nd_2Fe_{14}B$ to the exchange-correlation functional, for example, LDA + OC, GGA + OC, and GGA + U. The $4f$ electrons of Nd are considered explicitly as the valence in the case of GGA + U. We checked that changing U does not affect the magnetic moment of $Nd_2Fe_{14}B$ and the shape of the DOS except for the position of the sharp peaks derived from the $4f$ electrons in Nd. Thus, U is set to 6 eV for the $4f$ electrons of Nd used in the previous studies [33–35]. Figure 8 shows the DOS of $Nd_2Fe_{14}B$ calculated with LDA + OC, GGA + OC, and GGA + U. We set the lattice parameters of $Nd_2Fe_{14}B$ as the calculated ones with GGA + OC for comparison. The sharp blue peaks around −5, 2, and 4.5 eV

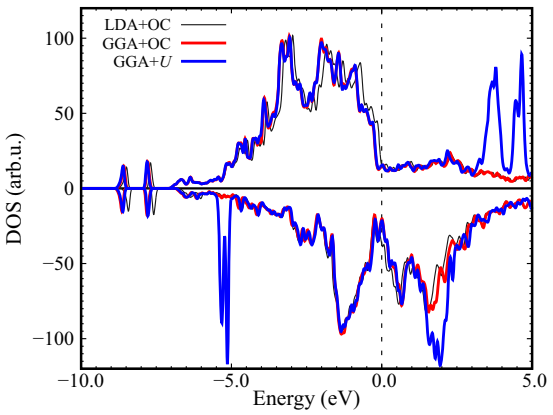

FIG. 8. The density of states of $Nd_2Fe_{14}B$ calculated with LDA + OC, GGA + OC, and GGA + U.

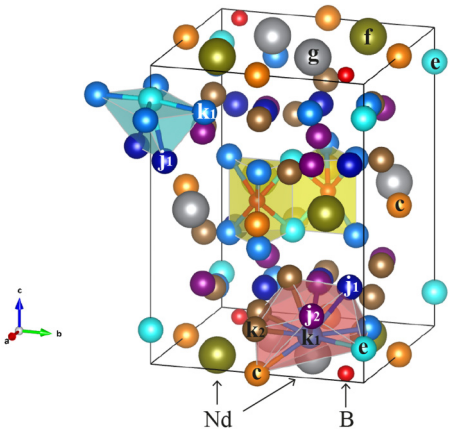

FIG. 9. The crystal structure of $Nd_2Fe_{14}B$ with the labels of Wyckoff positions. The cobaltized Fe atoms bond with B in the yellow regions. Magnetic moments are enhanced near the $4e$ and $16k_1$ sites highlighted as the blue and red regions, respectively.

that can be seen in the case of GGA + U come from the well-localized $4f$ electrons. The calculated magnetic moment and the lattice parameters of $Nd_2Fe_{14}B$ with GGA + U are consistent with experimental reports. The shapes of the DOS calculated with GGA + OC and GGA + U are essentially the same except for the sharp peaks coming from $4f$ electrons, although the OC pseudopotential of Nd does not consider the orbital hybridization between $4f$ and other electrons. This figure tells us that the hybridization effect between Nd $4f$ and other electrons is negligible. Furthermore, the magnetic moment and magnetization of $Nd_2Fe_{14}X$ calculated with LDA + OC, GGA + OC, and GGA + U show the same tendency. Therefore, this result supports us to use the open-core potential of Nd as a cheaper calculation cost alternative to GGA + U to calculate the electronic and magnetic structures of $Nd_2Fe_{14}X$.

APPENDIX B: LATTICE CONSTANTS

The calculated lattice constants and inner coordinates of $Nd_2Fe_{14}X$ (X = B, C, N, O, F) and Nd_2Fe_{14} are listed in Tables II and III, respectively. Figure 9 shows the crystal structure of $Nd_2Fe_{14}B$ with the labels of Wyckoff positions listed in Table III. The calculated lattice constants of $Nd_2Fe_{14}B$ listed in Table II are consistent with experimental values ($a \simeq 8.8$ Å, $c \simeq 12.2$ Å) [22,24,25]. Volume expansion due to added elements can be seen in all $Nd_2Fe_{14}X$ systems compared to Nd_2Fe_{14}. The lattice parameters c become shorter when B is replaced by C and N and become longer as X = O and F. This tendency might be related to the p-d hybridization between X and the neighboring Fe at the $16k_1$ and $4e$ sites.

X and the neighboring Fe align along the c axis rather than the a axis and c can reflect the bond length between X and Fe. From X = B to N, the atomic radius decreases [36]; thus, the bond length becomes shorter.

TABLE III. The inner coordinates for $Nd_2Fe_{14}X$ and Nd_2Fe_{14}.

Compound	Atom	Site	x	y	z
$Nd_2Fe_{14}B$	Nd	$4f$	0.266	0.266	0.0
		$4g$	0.142	−0.142	0.0
	Fe	$16k_1$	0.225	0.567	0.127
		$16k_2$	0.037	0.360	0.177
		$8j_1$	0.098	0.098	0.205
		$8j_2$	0.317	0.317	0.246
		$4e$	0.5	0.5	0.114
		$4c$	0.0	0.5	0.0
	B	$4g$	0.375	−0.375	0.0
$Nd_2Fe_{14}C$	Nd	$4f$	0.257	0.257	0.0
		$4g$	0.142	−0.142	0.0
	Fe	$16k_1$	0.225	0.566	0.120
		$16k_2$	0.036	0.359	0.177
		$8j_1$	0.098	0.098	0.209
		$8j_2$	0.317	0.317	0.245
		$4e$	0.5	0.5	0.107
		$4c$	0.0	0.5	0.0
	C	$4g$	0.374	−0.374	0.0
$Nd_2Fe_{14}N$	Nd	$4f$	0.254	0.254	0.0
		$4g$	0.142	−0.142	0.0
	Fe	$16k_1$	0.225	0.565	0.120
		$16k_2$	0.036	0.359	0.178
		$8j_1$	0.098	0.098	0.209
		$8j_2$	0.317	0.317	0.244
		$4e$	0.5	0.5	0.106
		$4c$	0.0	0.5	0.0
	N	$4g$	0.371	−0.371	0.0
$Nd_2Fe_{14}O$	Nd	$4f$	0.252	0.252	0.0
		$4g$	0.146	−0.146	0.0
	Fe	$16k_1$	0.224	0.562	0.129
		$16k_2$	0.035	0.360	0.177
		$8j_1$	0.098	0.098	0.204
		$8j_2$	0.316	0.316	0.244
		$4e$	0.5	0.5	0.117
		$4c$	0.0	0.5	0.0
	O	$4g$	0.363	−0.363	0.0
$Nd_2Fe_{14}F$	Nd	$4f$	0.258	0.258	0.0
		$4g$	0.146	−0.146	0.0
	Fe	$16k_1$	0.224	0.563	0.141
		$16k_2$	0.036	0.362	0.174
		$8j_1$	0.098	0.098	0.197
		$8j_2$	0.317	0.317	0.246
		$4e$	0.5	0.5	0.135
		$4c$	0.0	0.5	0.0
	F	$4g$	0.369	−0.369	0.0
Nd_2Fe_{14}	Nd	$4f$	0.256	0.256	0.0
		$4g$	0.139	−0.139	0.0
	Fe	$16k_1$	0.229	0.566	0.120
		$16k_2$	0.035	0.360	0.177
		$8j_1$	0.098	0.098	0.210
		$8j_2$	0.316	0.316	0.245
		$4e$	0.5	0.5	0.103
		$4c$	0.0	0.5	0.0

TABLE IV. The calculated $A_l^m\langle r^l\rangle$ of Nd at the $4f$ and $4g$ sites in $Nd_2Fe_{14}X$ (X = B, C, N, O, F) and Nd_2Fe_{14}. They are described in kelvin.

	$A_2^0\langle r^2\rangle$	$A_2^{-2}\langle r^2\rangle$	$A_4^0\langle r^4\rangle$	$A_4^{-2}\langle r^4\rangle$	$A_4^4\langle r^4\rangle$	$A_6^0\langle r^6\rangle$	$A_6^{-2}\langle r^6\rangle$	$A_6^4\langle r^6\rangle$	$A_6^{-6}\langle r^6\rangle$
					Nd($4f$)				
$Nd_2Fe_{14}B$	220	442	−21	−17	−18	2.6	1.5	−3.0	0.0
$Nd_2Fe_{14}C$	292	579	−23	−54	−37	4.1	7.9	2.9	4.7
$Nd_2Fe_{14}N$	336	627	−26	−73	−50	4.2	10.0	1.9	10.1
$Nd_2Fe_{14}O$	405	652	−28	−46	−59	4.5	6.5	7.4	15.3
$Nd_2Fe_{14}F$	459	691	−23	−12	−45	4.0	−1.1	10.6	15.9
Nd_2Fe_{14}	206	372	−19	−71	−34	4.3	7.9	−1.0	11.4
					Nd($4g$)				
$Nd_2Fe_{14}B$	331	−327	−30	−28	34	3.4	−3.2	3.0	11.9
$Nd_2Fe_{14}C$	387	−431	−33	−34	47	3.5	1.5	10.2	0.8
$Nd_2Fe_{14}N$	444	−532	−36	−36	58	2.9	4.2	14.1	−4.0
$Nd_2Fe_{14}O$	435	−562	−32	−70	−13	1.9	5.1	6.4	0.7
$Nd_2Fe_{14}F$	477	−658	−28	−68	33	2.0	6.0	7.7	6.8
Nd_2Fe_{14}	434	−308	−34	23	16	3.2	2.6	8.1	−0.3

At X = O, the antibonding state starts to be occupied and the occupation weakens the covalent bond between X and Fe. As a result, c in $Nd_2Fe_{14}O$ and $Nd_2Fe_{14}F$ become longer. An analogous trend is also observed in $NdFe_{11}TiX$ [18].

APPENDIX C: CRYSTAL-FIELD PARAMETERS

In this Appendix, we discuss the crystal-field parameters $A_l^m\langle r^l\rangle$ of Nd. The large magnetocrystalline anisotropy of $Nd_2Fe_{14}B$ is attributed to well-localized Nd $4f$ electrons with large orbital moments. In crystal-field theory, the magnetocrystalline anisotropy energy $E_{\rm MAE}(\theta,\varphi)$ of Nd in $Nd_2Fe_{14}X$ reads from the crystal-field Hamiltonian $\mathcal{H}_{\rm CEF}$:

$$E_{\rm MAE}(\theta,\varphi) = \langle J, M=-J|\mathcal{H}_{\rm CEF}|J, M=-J\rangle \quad \text{(C1)}$$

$$= \sum_{lm} \Theta_l A_l^m\langle r^l\rangle f_l(J)\frac{Z_l^m(\theta,\varphi)}{a_{lm}}, \quad \text{(C2)}$$

where

$$f_2 = J\left(J-\frac{1}{2}\right), \quad f_4 = J\left(J-\frac{1}{2}\right)(J-1)\left(J-\frac{3}{2}\right),$$
$$f_6 = J\left(J-\frac{1}{2}\right)(J-1)\left(J-\frac{3}{2}\right)(J-2)\left(J-\frac{5}{2}\right), \quad \text{(C3)}$$

$$\Theta_2 = -\frac{7}{3^2\times 11^2}, \quad \Theta_4 = -\frac{2^3\times 17}{3^3\times 11^3\times 13},$$
$$\Theta_6 = -\frac{5\times 17\times 19}{3^3\times 7\times 11^3\times 13^2}, \quad \text{(C4)}$$

$$a_{2-2} = a_{22} = \frac{1}{4}\sqrt{\frac{15}{\pi}}, \quad a_{20} = \frac{1}{4}\sqrt{\frac{5}{\pi}},$$
$$a_{4-4} = a_{44} = \frac{3}{16}\sqrt{\frac{35}{\pi}}, \quad a_{4-2} = a_{42} = \frac{3}{8}\sqrt{\frac{5}{\pi}},$$
$$a_{40} = \frac{3}{16}\sqrt{\frac{1}{\pi}}, \quad a_{6-6} = a_{66} = \frac{231}{64}\sqrt{\frac{26}{231\pi}},$$

TABLE V. The comparison of the calculated $A_l^m\langle r^l\rangle$ with previous theoretical [38,40] and experimental [37] studies for $Nd_2Fe_{14}B$. They are described in kelvin. In Ref. [38], the notation of the Nd sites, $4f$ and $4g$, are opposite from the present notation, and here it is alternated to compare with our data. The data for Nd1 and Nd2 on the middle layer described in Ref. [40] correspond to Nd($4f$) and Nd($4g$), respectively. The data in Ref. [37] are shown as A_l^m [K$a_{\rm B}^{-l}$] itself, and we multiply $\langle r^2\rangle = 1.001a_{\rm B}^2$, $\langle r^4\rangle = 2.401a_{\rm B}^4$, and $\langle r^6\rangle = 12.396a_{\rm B}^6$, to the values of A_l^m, respectively [41]. Nd($4f$) and Nd($4g$) sites are not distinguished in Ref. [37]. For $A_2^{-2}\langle r^2\rangle$ and $A_6^{-6}\langle r^6\rangle$, the values at Nd($4f$) and Nd($4g$) on one plane are the same magnitude of each Nd on the plane shifted by $0.5c$ with opposite signs.

		$A_2^0\langle r^2\rangle$	$A_2^{-2}\langle r^2\rangle$	$A_4^0\langle r^4\rangle$	$A_4^{-2}\langle r^4\rangle$	$A_4^4\langle r^4\rangle$	$A_6^0\langle r^6\rangle$	$A_6^{-2}\langle r^6\rangle$	$A_6^4\langle r^6\rangle$	$A_6^{-6}\langle r^6\rangle$
Present	Nd($4f$)	220	442	−21	−17	−18	2.6	1.5	−3.0	0.0
	Nd($4g$)	331	−327	−30	−28	34	3.4	−3.2	3.0	11.9
Calc. [38]	Nd($4f$)	323	807	−50	−85	−117	−2.7	3.9	−24	0.1
	Nd($4g$)	540	−727	−54	82	125	−2.2	0.3	−15	5
Calc. [40]	Nd($4f$)	442	777	−28	−69	−106	17	−2	156	57
	Nd($4g$)	605	−286	−35	84	96	13	2	79	11
Expt. [37]		295	−454	−29.5			−22.8	121	−197	

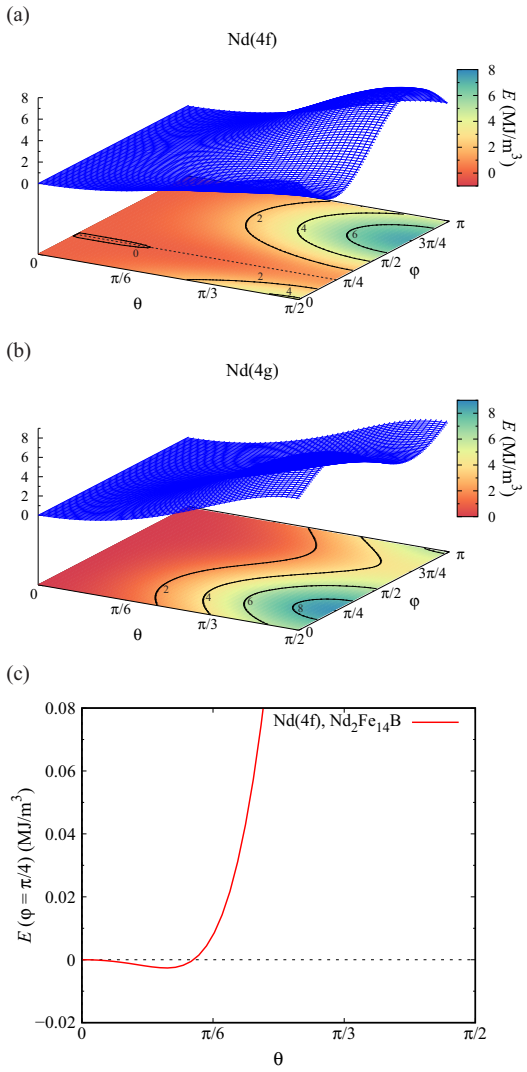

FIG. 10. The spin-angle dependence of MAE for (a) Nd($4f$) and (b) Nd($4g$) in $Nd_2Fe_{14}B$. The solid lines with numbers in the color map represent the contour lines of MAE. The dashed line is a guide to the eye for the data in (c). (c) The angle dependence of MAE for Nd($4f$) in $Nd_2Fe_{14}B$ at $\varphi = \pi/4$.

$$a_{6-4} = a_{64} = \frac{21}{32}\sqrt{\frac{13}{7\pi}}, \quad a_{6-2} = a_{62} = \frac{1}{64}\sqrt{\frac{2730}{\pi}},$$
$$a_{60} = \frac{1}{32}\sqrt{\frac{13}{\pi}}. \tag{C5}$$

This formulation is referred to in Ref. [37]. Constant parameters are the Stevens factor Θ_l and f_l in which the total angular momentum J $(= L + S)$ is 9/2 $(L = 6, S = 3/2)$ for Nd. Z_l^m is a real spherical harmonic. $A_l^m\langle r^l\rangle$ are crystal-field parameters at the Nd site. Here l takes 2, 4, or 6, and m is an even number from $-l$ to l:

$$A_l^m\langle r^l\rangle = a_{lm}\int_0^{r_c} dr r^2 |R_{4f}(r)|^2 V_{lm}(r). \tag{C6}$$

We use the effective potential $V_{lm}(r)$ of Nd atoms obtained by solving the Kohn-Sham equation self-consistently. r_c is a cutoff radius which is determined by Bader analysis as in Ref. [18], and $R_{4f}(r)$ is an atomic radial function of the Nd $4f$ electrons. The results for $A_l^m\langle r^l\rangle$ of Nd at the $4f$ and $4g$ sites in $Nd_2Fe_{14}X$ and Nd_2Fe_{14} are summarized in Table IV. The comparison with the previous calculation [38] and experiment [37] is also shown for $Nd_2Fe_{14}B$ in Table V. The order of magnitude for $l = 2$ and 4 agrees with the previous calculated values, and the sign for them also agrees, except for $(l, m) = (4, -2)$ of Nd($4g$).

Figures 10(a) and 10(b) show the angle dependence of Eq. (C2) for Nd($4f$) and Nd($4g$) in $Nd_2Fe_{14}B$. Strong dependence on the azimuthal angle φ can be seen in the magnetocrystalline anisotropy energy (MAE) for both Nd($4f$) and Nd($4g$). Figure 10(c) shows the MAE at $\varphi = \pi/4$ for Nd($4f$). The negative region appears around $\theta = 0$. We here note that the exchange coupling with Fe is not taken into account and that such a small contribution of MAE may not survive in the presence of the strong exchange coupling. Therefore, we cannot conclude the existence of the spin canting at low temperatures from the present result [39]. However, it indicates the importance of the azimuthal angle dependence of the MAE to describe the spin configuration at low temperature.

[1] P. Gubbens, A. van der Kraan, and K. Buschow, Physica B+C (Amsterdam) **86–88**, 199 (1977).
[2] H. Bo-Ping and J. M. D. Coey, J. Less-Common Met. **142**, 295 (1988).
[3] F. Weitzer, K. Hiebl, and P. Rogl, J. Appl. Phys. **65**, 4963 (1989).
[4] M. Sagawa, S. Fujimura, N. Togawa, H. Yamamoto, and Y. Matsuura, J. Appl. Phys. **55**, 2083 (1984).
[5] http://www.japanprize.jp/data/prize/commemorative_lec_2012_e.pdf
[6] M. Sagawa, S. Fujimura, H. Yamamoto, Y. Matsuura, and S. Hirosawa, J. Appl. Phys. **57**, 4094 (1985).
[7] J. Kanamori, Prog. Theor. Phys. Suppl. **101**, 1 (1990).
[8] J. Kanamori, Trans. Magn. Soc. Jpn. **1**, 1 (2001).
[9] J. Kanamori, J. Alloys Compd. **408**, 2 (2006).
[10] H. Hasegawa and J. Kanamori, J. Phys. Soc. Jpn. **33**, 1607 (1972).
[11] N. Hamada, J. Phys. Soc. Jpn. **46**, 1759 (1979).
[12] S. Asano and M. Yamaguchi, Phys. B (Amsterdam, Neth.) **237**, 541 (1997).
[13] M. Yamaguchi and S. Asano, Phys. B (Amsterdam, Neth.) **254**, 73 (1998).
[14] T. Ozaki, Phys. Rev. B **67**, 155108 (2003).
[15] J. P. Perdew, K. Burke, and M. Ernzerhof, Phys. Rev. Lett. **77**, 3865 (1996).
[16] http://qmas.jp/
[17] T. Miyake, K. Terakura, Y. Harashima, H. Kino, and S. Ishibashi, J. Phys. Soc. Jpn. **83**, 043702 (2014).
[18] Y. Harashima, K. Terakura, H. Kino, S. Ishibashi, and T. Miyake, Phys. Rev. B **92**, 184426 (2015).

[19] J. F. Herbst, J. J. Croat, F. E. Pinkerton, and W. B. Yelon, Phys. Rev. B **29**, 4176 (1984).
[20] C. B. Shoemaker, D. P. Shoemaker, and R. Fruchart, Acta Crystallogr. C **40**, 1665 (1984).
[21] D. Givord, H. Li, and J. Moreau, Solid State Commun. **50**, 497 (1984).
[22] J. F. Herbst, Rev. Mod. Phys. **63**, 819 (1991).
[23] D. Givord, H. S. Li, and F. Tasset, J. Appl. Phys. **57**, 4100 (1985).
[24] M. Sagawa, S. Hirosawa, H. Yamamoto, S. Fujimura, and Y. Matsuura, Jpn. J. Appl. Phys. **26**, 785 (1987).
[25] O. Isnard, W. B. Yelon, S. Miraglia, and D. Fruchart, J. Appl. Phys. **78**, 1892 (1995).
[26] K. H. J. Buschow, Rep. Prog. Phys. **54**, 1123 (1991).
[27] R. Sasaki, D. Miura, and A. Sakuma, Appl. Phys. Express **8**, 043004 (2015).
[28] Y. Toga, M. Matsumoto, S. Miyashita, H. Akai, S. Doi, T. Miyake, and A. Sakuma, Phys. Rev. B **94**, 174433 (2016).
[29] K.-D. Durst and H. Kronmüller, J. Magn. Magn. Mater. **59**, 86 (1986).
[30] Y. Tatetsu, S. Tsuneyuki, and Y. Gohda, Phys. Rev. Appl. **6**, 064029 (2016).
[31] Z. Torbatian, T. Ozaki, S. Tsuneyuki, and Y. Gohda, Appl. Phys. Lett. **104**, 242403 (2014).
[32] H. Akai, M. Takeda, M. Takahashi, and J. Kanamori, Solid State Commun. **94**, 509 (1995).
[33] S. L. Dudarev, G. A. Botton, S. Y. Savrasov, C. J. Humphreys, and A. P. Sutton, Phys. Rev. B **57**, 1505 (1998).
[34] N. Singh, S. M. Saini, T. Nautiyal, and S. Auluck, J. Appl. Phys. **100**, 083525 (2006).
[35] I. Kitagawa and Y. Asari, Phys. Rev. B **81**, 214408 (2010).
[36] P. Pyykkö, Phys. Rev. B **85**, 024115 (2012).
[37] M. Yamada, H. Kato, H. Yamamoto, and Y. Nakagawa, Phys. Rev. B **38**, 620 (1988).
[38] K. Hummler and M. Fähnle, Phys. Rev. B **53**, 3290 (1996).
[39] S. Hirosawa, Y. Matsuura, H. Yamamoto, S. Fujimura, M. Sagawa, and H. Yamauchi, J. Appl. Phys. **59**, 873 (1986).
[40] T. Yoshioka, H. Tsuchiura, and P. Novák, Mater. Res. Innovations **19**, S4 (2015).
[41] A. J. Freeman and R. E. Watson, Phys. Rev. **127**, 2058 (1962).